Nanoscale

Accepted Manuscript

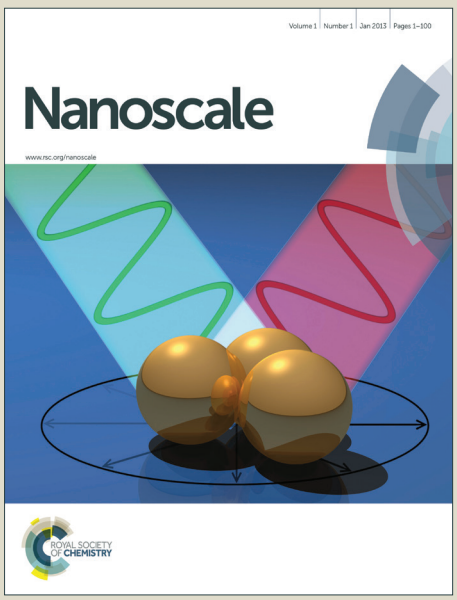

ROYAL SOCIETY OF CHEMISTRY

www.rsc.org/nanoscale

Higher-Power Supercapacitor Electrodes Based on Mesoporous Manganese Oxide Coating on Vertically Aligned Carbon Nanofibers

Steven A. Klankowski[a], *Gaind P. Pandey*[a], *Gary Malek*[b], *Conor R. Thomas*[c], *Steven L. Bernasek*[c], *Judy Wu*[b], *and Jun Li*[a,*]

[a]Department of Chemistry, Kansas State University, Manhattan, KS 66506, USA.

[b]Department of Physics and Astronomy, University of Kansas, Lawrence, KS 66045, USA

[c]Department of Chemistry, Princeton University, Princeton, NJ 08544, USA

[*]Corresponding Author: **Jun Li** Email: **junli@ksu.edu**

Abstract

A study on the development of high-power supercapacitor materials based on formation of thick mesoporous MnO_2 shells on a highly conductive 3D template using vertically aligned carbon nanofibers (VACNFs). Coaxial manganese shells of 100 to 600 nm nominal thicknesses are sputter-coated on VACNFs and then electrochemically oxidized into rose-petal-like mesoporous MnO_2 structure. Such a 3D MnO_2/VACNF hybrid architecture provides enhanced ion diffusion throughout the whole MnO_2 shell and yields excellent current collection capability through the VACNF electrode. These two effects collectively enable faster electrochemical reactions during charge-discharge of MnO_2 in 1 M Na_2SO_4. Thick MnO_2 shells (up to 200 nm in radial thickness) can be employed, giving a specific capacitance up to 437 F g^{-1}. More importantly, supercapacitors employing such a 3D MnO_2/VACNF hybrid electrode illustrate more than one order of magnitude higher specific power than the state-of-the-art ones based on other MnO_2 structures (reaching ~240 kW kg^{-1}) while maintaining a comparable specific energy in the range of 1 to 10 Wh kg^{-1}. This hybrid approach demonstrates the potential of 3D core-shell architectures for high-power energy storage devices.

Keywords: Manganese oxide, carbon nanofibers, hybrid electrode materials, supercapacitor, electrical energy storage

Nanostructured materials have garnered significant attention for application as high-performance electrodes in electrochemical capacitors (ECs), also known as supercapacitors, due to the benefits of increased surface area, high porosity, and enhanced electrochemical surface activity. Exploiting these attributes, supercapacitors are now capable of delivering high specific energy approaching that of batteries. More importantly, supercapacitors can be charged and discharged at much higher power rates than batteries, effectively positioning themselves in the diagonal of the Ragone plane.[1] Depending on the specific charge storage mechanisms and the electrode materials, supercapacitors are normally divided into two classes: electric double layer capacitors (EDLCs) and pseudo-capacitors. EDLCs rely on the high surface area of chemically stable electrode materials to store significant amounts of charge at the electrode/electrolyte interfaces, providing rapid charge-discharge capabilities. Activated carbons are the most commonly used EDLC electrode materials with a specific surface area (SSA) up to ~3000 $m^2 g^{-1}$ and good electrical conductivity in the range of 2-20 S cm^{-1}.[2-4] In addition, more sophisticated porous structures are being intensively studied to further enhance the performance.[2, 3, 5] Conversely, pseudo-capacitors rely on faradaic reactions involving electrochemical charge-transfer processes similar to those in batteries, but are confined at or near the surface of redox-active solid electrode materials to achieve fast and reversible reactions. Transition metal oxides (e.g. RuO_2, MnO_2, TiO_2, Fe_2O_3, VO_x, etc.) and a family of conducting polymers (e.g. polypyrrole, polyaniline) are most commonly used pseudo-capacitor electrode materials.[2, 6] While the potential charge storage capability (and thus specific energy) of pseudocapacitors is significantly higher than that of EDLCs, their charge-discharge rate (and thus specific power) is often limited by the reaction kinetics. Much of recent research is focused on developing hybrid nanostructured materials for high-performance supercapacitors that blend the high SSA and efficient current collection capability of EDLC materials with fast surface redox reactions of pseudo-capacitor materials so that both high specific energy and high power rate can be obtained.[2, 7]

Hydrous ruthenium oxide (RuO_2) is one of the foremost supercapacitor electrode material due to its high theoretical specific capacitance (SC) (>1,300 F g^{-1}), high electrical conductivity (~1 x 10^2 S cm^{-1}), and long-term cycle stability.[8] However, due to the high production cost and known environmental toxicity, practical applications of RuO_2 have been limited and other materials are being actively pursued as alternatives. Among them, manganese oxides (MnOx) have received the most attention in part due to their abundance, low cost and benign nature. The theoretical SC value of MnO_2 is 1,370 F g^{-1} for a redox process involving one electron per Mn atom,[9] which is comparable to hydrous RuO_2 in terms of reaction mechanism. MnO_2 is also very similar to RuO_2 with its pseudo-capacitance behavior derived via proton or alkali metal cation (C^+) insertion into the lattice structure during reduction processes[9, 10]:

$$MnO_2 + e^- + H^+ \leftrightarrow MnOOH, \quad (1)$$

$$MnO_2 + e^- + C^+ \leftrightarrow MnOOC, \quad (2)$$

with the cation C^+ being K^+, Na^+, or Li^+. Additionally, it has been proposed that surface adsorption of electrolyte cations C^+ may also contribute[10] through:

$$MnO_2 + e^- + C^+ \leftrightarrow (MnO_2^-C^+)_{surface} \quad (3)$$

with the reaction rate determined by the balance of electron and ion transport rates in the electrode materials. Despite the likeness in reaction mechanisms, MnO_2 (and many other metal oxides) has a much lower electrical conductivity than RuO_2 (with σ_{MnO_2} = ~10^{-5}-10^{-6} S cm^{-1} versus σ_{RuO_2} = ~1 x 10^2 S cm^{-1}, differentiated by 7-8 orders of magnitude) [11, 12] while the diffusion coefficients of protons and alkali cations in MnO_2 (D_{H^+} = 6 x 10^{-10} cm^2 s^{-1} and D_{Na^+} = ~ 5 x 10^{-10} cm^2 s^{-1})[9, 13] are greater than those in RuO_2 (D_{H^+} = 5 x 10^{-14} cm^2 s^{-1}).[11, 14-17] Overall, the effective reaction rate in the bulk MnO_2 material was found to be much less than its RuO_2 counterpart because only a limited fraction of bulk MnO_2 was electrically connected and active in electrochemical reactions.[9] The low electrical conductivity also restrained the applicable power rate of the bulk MnO_2 electrodes.

To date, the highest reported SC value of 1,380 F g^{-1} for MnO_2 was measured at a very slow scan rate of 5 mV s^{-1}, [9]which is not meaningful for practical applications and opts to be augmented by other redox reactions. Making MnO_2 into thinner films and incorporating binders and conductive additives have been adopted to improve the overall rate performance, but this always comes at the expense of the total specific energy. In particular, due to the sluggish proton and cation diffusion rates, the electrochemical reaction of MnO_2 may be limited to the surface layer of only several nanometers at fast charge-discharge rates (on a timescale of seconds), which significantly reduces the obtainable specific capacitance.[2, 9, 13] Hence, for MnO_2-based electrodes to outperform RuO_2-based supercapacitors, the electrode design must provide a very high active surface area along with effective electrical connectivity through the entire MnO_2 material while maintaining electrode robustness to endure tens-of-thousands of charge-discharge cycles. MnO_2 were also synthesized in various nanostructures to improve its electrochemical performance as supercapacitor electrode materials.[18-20]

One promising approach to fulfilling the above requirements is to create a three-dimensional (3D) core-shell hybrid architecture consisting of thin MnO_2 shells on stable conductive nanostructured cores.[11] Carbon nanotubes (CNTs), due to the nanoscale fiber-like structure, high electrical conductivity, and good chemical stability, have been recognized as an attractive core material to improve current collection, as demonstrated in the intensive studies of CNTs as EDLC materials.[2, 3] Various CNT/MnO_2 composites[21-24] or thin MnO_2 coating on dense, randomly stacked CNT films[25-27] have demonstrated rather high SC value varying from ~100 to ~600 F g^{-1} at scan rates up to hundreds of millivolts per second in cyclic voltammetry (CV) or at current density up to tens of amperes per gram in galvanostatic charge-discharge measurements. Generally, only ultrathin MnO_2 coatings of a few nanometers on CNT surfaces can afford both the high SC and high charge-discharge rates, which would only be limited by the high contact resistance between CNTs. In fact, the MnO_2 coating sandwiched between CNT films would make the overall film resistance even higher.

Alternatively, vertically aligned CNTs were explored as a binder-free 3D current collector where all CNTs were directly anchored on a common conductive surface.[28, 29] MnO_2 has been electrochemically deposited as flower-like nanoparticles along the CNTs [28] or filled between CNTs.[29] However, the SC value and charge-discharge rate are not much better than the randomly stacked CNTs. In contrast, we have previously demonstrated another type of 3D hybrid architecture based on electrodeposition of a uniform 7.5-nm compact MnO_2 film on vertically aligned carbon nanofibers (VACNFs).[30] VACNFs are a special type of multi-walled CNTs grown by plasma enhanced chemical vapor deposition (PECVD), which consist of a stack of conical graphitic cups instead of concentric seamless tubes.[31-34] The abundant active broken graphitic edges at the sidewall of VACNFs were found to be the key in enabling uniform MnO_2 deposition and formation of an effective electrochemical interface.[30] As a result, a high SC value of ~350 F g^{-1} was obtained at high scan rates up to 2,000 mV s^{-1}. However, the SC value tended to decrease as a thicker MnO_2 was deposited, limiting the overall energy density.[30] This was attributed to the higher electrical resistance and slower mass transport across the thicker compact MnO_2 layers. Here we extend this unique core-shell electrode architecture to much thicker MnO_2 coatings, over ~200 nm in radial thickness. Particularly, a mesoporous manganese oxide shell with nanoscale rose-petal-like structure was formed by electrochemical oxidation of the sputtered Mn shell on the VACNF scaffold, as illustrated in Figures 1a & 1b. The mesoporous MnO_2 structure provides a significantly enhanced solid/liquid interface inside a larger electrode volume, allowing protons and other cations to access the whole MnO_2 material through fast diffusion in solution instead of moving across the solid MnO_2 materials. The ion diffusion length across the MnO_2 plane is less than ~ 10 nm. Consequently, a remarkable high-rate performance was obtained.

FIGURE 1

Experimental

VACNFs Growth and Mn-shell Deposition

An oxygen-free titanium foil with the thickness of 25 μm (Titanium Grade 2, Hamilton Precision Metals, PA) was cut to a 15 cm x 15 cm sheet. A 300 nm thick chromium barrier layer followed by a 30 nm nickel catalyst layer were deposited using a high-vacuum Perkin Elmer 4400 series magnetron sputtering system at UHV Sputtering Inc. (Morgan Hill, CA). This Ni/Cr/Ti sheet was then cut into disks of 18 mm in diameter for test cell use. VACNFs with an average length of 5.0 μm and an average diameter of 150 nm were grown on the Ti foils using a DC-biased PECVD system (AIXTRON, CA) following a similar procedure in literature.[32, 33, 35] An areal density of ~1.1×10^9 CNFs cm^{-2} was achieved. Pure Mn (99.95%, ACI Alloy) was deposited on the individual disks of VACNF arrays using a custom built sputtering chamber. The substrate was mounted in an on-axis configuration relative to the sputtering gun. Before Mn deposition, the chamber was flushed with nitrogen gas (99.999%) and then pumped down to a base pressure of ~10^{-6} Torr. It was then filled with argon gas (99.999%) to a pressure of approximately 20 mTorr. The Mn target was pre-sputtered for three minutes to expose a fresh surface. Sputtering was conducted at room temperature with a power of 48 W and at a rate of approximately 0.67 nm s^{-1} as determined by profilometry (KLA Tencor P-16 Profiler). The nominal thicknesses of Mn was controlled in the range of 50 nm to 600 nm, which was further confirmed with the scanning electron microscopy (SEM) by inspection of the cross-section of the Mn films deposited on reference Ti foils without VACNFs.

Electrochemical Oxidation and Charge/Discharge Tests

The electrochemical oxidation and cycling tests of the Mn-coated VACNF arrays were performed using a Teflon cell sealed against the Mn-coated VACNF array with an O-ring, leaving a total area of 1.39 cm^2 exposed. The electrolyte for this experiment was 1.0 M Na_2SO_4 solution prepared with 18.2 MΩ deionized water. All measurements were conducted by a three-electrode configuration in 6.0 mL of electrolyte with the Mn or MnO_2-coated VACNF array as the working electrode, an Ag/AgCl (4 M

KCl) reference electrode, and a Pt foil counter electrode. The initial Mn coating was oxidized by chronopotentiometry method from the open circuit potential (~ –1.3 V) to the maximum potential of +0.9 V vs Ag/AgCl (4 M KCl). The electrolyte was quickly replaced with new solution after oxidation and CV measurements were then performed from 0.0 V to 0.8 V with a scan rate varying from 1.0 mV s^{-1} to 2000 mV s^{-1}. Chronopotentiometric charge/discharge tests were performed at various currents from 0.56 A g^{-1} to 1115 A g^{-1} (88.3 μA to 176.7 mA total, respectively). Electrochemical impedance spectroscopy (EIS) measurements were performed from 100 kHz to 10 mHz, at an amplitude of 5.0 mV and a bias of 0.4 V. All electrochemical measurements were conducted with a CHI 760D Electrochemical Workstation (CH Instruments, *Austin, TX*).

Electron Microscopy and X-ray Photoelectron Spectroscopy (XPS) Characterization

The structures of the electrodes before and after electrochemical testing were examined by SEM (FEI Nano 430), and transmission electron microscopy (TEM) (FEI Tecnai F20 XT). All electrodes were removed from Teflon cell in the discharged state (0.0 V), rinsed with copious amounts of deionized water to remove any remaining Na_2SO_4 salt from the electrode**,** and dried in a vacuum oven at ambient temperature. Surface analysis was done by XPS using the VG ESCALAB MkII system with a Phi 04-548 dual anode X-ray source. A Mg Kα line (1253.6 eV) generated at 15 kV and 300 W was used in this study. Survey scans used a pass energy of 100 eV, a step of 0.5 eV, and a dwell time of 200 ms. High-resolution core-level scans employed a pass energy of 20 eV, a step of 0.05 eV, and a dwell time of 500 ms.

Results and Discussion

Structural Characterization MnO_2-VACNF Electrode

As demonstrated in our earlier studies,[30, 35, 36] the VACNF array provides a unique 3D platform to support a variety of active materials that can be deposited onto to the CNFs by either physical or chemical methods. With their unique cup-stacking graphitic structure and a diameter of 100-200 nm,

the individual CNFs provide a mechanically robust scaffold, able to retain the integrity during Mn deposition and subsequent wet electrochemical processes. The CNFs are well separated and vertically aligned, forming a non-entangled brush-like structure that provides a stable Ohmic contact with the substrate.[31, 33, 34] The CNFs are known for excellent electrical conductivity along the axis (~2.5×10^3 S cm^{-1}, about 25 fold of the conductivity of RuO_2), serving to facilitate fast electron transport to and from the active materials.[37] Unlike the smooth sidewalls of a CNT, the edges of the graphitic cups create surface irregularities along the fiber surface that facilitated nucleation of the Mn flux during sputtering and provided an active site for fast electron transfer at the Mn/CNF interface. The larger, open space between the VACNFs enabled greater amounts of Mn metal to be deposited onto each CNF, forming a thick coaxial shell that was both electrically and chemically connected to the CNF.

In this study, Mn metal at the nominal thickness of 100 nm, 200 nm, 300 nm, or 600 nm was sputtered onto the VACNF in order to obtain the maximum specific energy at high specific power. Figures 1c–f show representative SEM images of the as-sputtered Mn-coating (at 300 nm nominal thickness) on a VACNF array before (Figures 1c and 1e) and after electrochemical oxidation (Figures 1d and 1f). The Mn sputtering process deposited a coaxial shell consisting of Mn nanoparticles. At 100 nm nominal Mn deposition thickness, the Mn shell was found to be rather uniform along the CNFs, with a radial thickness of ~40 nm. At 300 and 600 nm nominal Mn deposition, the shell thickness increased to ~130 and ~200 nm, respectively (Figure S1). The Mn nanoparticles appeared to wrap along the whole length of CNFs but with larger shell thickness at locations nearer to the CNF tip where Mn flux was the greatest during deposition (Figures S1b, S1e, and S1h). The Mn nanoparticles appeared to be crystalline in-nature, with sizable facets and lattice edges broken up by small crevasses that penetrated deep to the core. All these features provided a large surface area and high porosity, which allowed the electrolyte to effectively access the whole Mn shell in the next step.

The Mn-coated VACNF electrodes were then oxidized in galvanostatic mode by applying a

current density of 127 μA cm^{-2} (177 μA total) starting at an open circuit potential (OCP) of about -1.3 V. The electropotential was monitored with chronopotentiometry until reaching the upper limit at +0.9 V. The oxidized Mn shell appeared billowy for the entire lot, with very intricate dendrites that resembled rose petals indiscriminately arranged on the VACNF sidewall (Figures 1d, 1f, and Figure S2). Such Mn oxide shells are highly porous, with very thin walls (~20 nm) extending out radially from the CNF core, forming a large expanded shell with cavernous pores across the whole Mn oxide layer. The 100 nm nominal coating showed a coarser structure, with large thick petals (Figures S2a-d), while the 600 nm coatings are more ornate with thinner and more convoluted petals (Figure S2i-l). The high porosity of the MnO_2 shell is expect to significantly improve the power density since ions can access to the whole MnO_2 film faster through diffusion in electrolyte solution and only need to transport < 10 nm across the solid MnO_2 material from both side of the petal plane.

FIGURE 2

Since the 1.0 M Na_2SO_4 electrolyte used for oxidation has a measured pH of 9.4 (unbuffered), the Pourbaix diagram for Mn (from Reference [38]) suggests oxidation occurs along the following pathway:

$$Mn(s) \xrightarrow{1} Mn(OH)_2 \xrightarrow{2} Mn_3O_4 \xrightarrow{3} Mn_2O_3 \xrightarrow{4} MnO_2 \qquad (4)$$

The average valence states of Mn in the above five species are 0, 2, 2.67, 3, and 4, respectively. Accordingly, four reaction steps were clearly observed in the chronopotentiometric oxidation profiles as shown in Figure 2a. The plateaus at characteristic potentials represent the transition of Mn from one predominant valence state to the next, with the potentials defined by the boundaries between ion species on the Pourbaix diagram at the electrolyte's pH.[2, 38, 39]

For example, the 600 nm sample starts with an OCP of -1.3 V. The potential rises to -1.0 V as Mn(s) is gradually oxidized to $Mn(OH)_2$, and then rises gradually up to 0.0 V representing the formation of Mn_3O_4, and to +0.1 V accompanying the transition from Mn_3O_4 to Mn_2O_3. The strongest

oxidation features are the transition from Mn_2O_3 to the final form of MnO_2 at +0.9 V. The time at each step represents the charge involved in the reaction. Interestingly, the thinner Mn coatings with 100 nm and 200 nm nominal thicknesses show smaller oxidation time in the first and second steps compared to that required to complete oxidation into MnO_2. Since the Mn coating on the VACNF is much thinner (~40 nm and ~80 nm, respectively) than the nominal thickness and has a greater surface area to mass ratio than thicker coatings, it is suspected that a significant portion of the Mn atoms have been partially oxidized to MnO or Mn_3O_4 due to exposure to air and the electrolyte before the electrochemical oxidation process. To confirm this, an effective oxidation state (EOS, n_{Mn}) was calculated from each chronopotentiometric profile using the following equation:

$$n_{Mn} = \frac{i\,t}{(m/M)\,F} \qquad (5)$$

where i is the applied current, t is the time required to complete the oxidation, M is the molar mass of Mn, m is the mass of involved Mn material, and F = 96,500 C mol^{-1} is the Faraday constant. The average EOS of the samples at four different nominal thicknesses is shown in Figure 2b. The curve shows an increasing trend toward a higher oxidation state from 2.3 to 3.6 to 3.8 to 4.2 as the nominal Mn thickness increases from 100 nm to 200 nm, 300 nm, and 600 nm, respectively, consistent with the expectation that thinner Mn coating has higher volume percentage being oxidized in the open air. The EOS of the 600 nm nominal Mn thickness is larger than 4 due to some side reactions (such as water electrolysis) between +0.8 to +0.9 V (as shown in CV in Figure 4a in later discussion). Thus we have set the upper potential limit at +0.8 V in later supercapacitor tests. These results indicate that even the Mn in the thick coating (at 600 nm nominal thickness) on the VACNF can be completely oxidized into MnO_2, the desired form for optimum supercapacitor performance. The 600 nm nominal thickness is much greater than those that can be applied as thin films on flat surfaces.[40, 41]

Further comparison between SEM images of Figures S1 and S2 show that the expansion of the Mn shell after electrochemical oxidation is smaller than expected. As shown in a control test utilizing

a 100 nm thick Mn film sputtered onto a flat Cr-coated silicon wafer, the Mn film thickness expanded by >100% after electrochemical oxidation to form the porous rose-petal-like structure, consistent with the previous report for larger film thicknesses.[41] Besides the large volume expansion, up to 0.10 mg of Mn may dissolute into the 6.0 mL of electrolyte, first in the form of Mn^{2+} (based on the calculation with K_{sp} = 1.9 x10^{-13} for $Mn(OH)_2$, see SI for details), during the electrochemical oxidation process. It then formed the species at other valence states with much lower solubility, evident by the electrolyte turning a brownish color. The Mn mass loss during oxidation process is significant for 100 nm nominal Mn thickness (to a maximum of ~63%), but is much less important as the film thickness is increased, dropping to a maximum value of ~10% for 600 nm nominal Mn thickness. It needs to be noted that the exact mass loss of Mn during oxidation varied for each sample, limited by many uncontrolled factors such as sample storage time in the air after Mn deposition, humidity, and oxidation current density. To make the calculations consistent, we neglect the mass loss and used the total starting Mn mass (and subsequent MnO_2 mass) for all samples in later energy storage studies. As a result, the performance in terms of specific energy and specific power may be under-estimated, particularly for samples with smaller nominal thickness.

TABLE 1

FIGURE 3

XPS surface analysis of MnO_2-VACNF Electrodes

The MnO_2-coated VACNF electrodes at different nominal Mn thicknesses were characterized by XPS to determine the actual valence state of the Mn after long charge-discharge cycles. The electrodes were polarized to 0.0 V before the potential control was turned off so that the MnO_2 was in the reduced form. The cell was then quickly dissembled and the electrodes were rinsed with deionized water (See Experimental Section). The survey spectra for all the electrode samples show Mn 2p (~642 eV), Mn 3s (~83-89 eV) and O 1s (529-533 eV) peaks attributed to manganese oxides. The Mn 3s core level

spectra splits into a doublet due to the parallel spin coupling of the 3s electron with the 3d electron during the photoelectron ejection.[9] The separation in the binding energy between these two peaks is related to the mean Mn oxidation state, as described previously.[42, 43] As shown in Figure 3a and Table 1, the splitting of the Mn 3s peak is almost the same for 100 nm and 300 nm samples (at 5.23 and 5.32 eV, respectively), indicating that the Mn valence state is about 3 according to literature.[9] In contrast, the splitting of the Mn 3s peak of the 600 nm sample is 4.64 eV, indicating that the valence state of Mn in this electrode is close to 4.[9] Since XPS only provides the information of a very thin layer (<5 nm) at the outer surface, it is likely that the valence state of Mn in deeper layer of this electrode is different. The O 1s spectra provide further information of Mn-O bonds and hydration contents. Figure 3b shows a representative O 1s spectrum of the 100 nm sample, which can be de-convoluted into three types of bonds: Mn-O-Mn (529.4 eV), Mn-O-H (530.9 eV) and H-O-H (532.3 eV). The peak areas of Mn-O-Mn and Mn-OH are very similar (at 40% and 38%, respectively), suggesting that nearly all Mn atoms at the surface formed MnOOH bonds during the reduction reaction described by Eq. 1. The third peak accounts for 22% of oxygen due to the adsorption of water. The Mn 3s and O 1s spectra of the 100 nm MnO_2/VACNF sample agree well with each other. But for thicker MnO_2-coated samples, the large adsorption of water and $NaSO_4$ salt in the mesoporous MnO_2 layer caused large uncertainties in the quantitative analysis of O 1s spectra.

FIGURE 4

Electrochemical Performance of MnO_2-VACNF Electrodes

After the oxidation step, the electrolyte was replaced with fresh solution and cyclic voltammetry was performed from 0.0 V to 0.8 V at the scan rate varying from 1 mV s^{-1} to 2000 mV s^{-1}. Figures 4a and 4b show the I-V curves of the four samples at two scan rates of 1 mV s^{-1} and 1000 mV s^{-1}, respectively. Similar data at 10 mV s^{-1}, 100 mV s^{-1}, and 2000 mV s^{-1} are shown in Figure S4. All four samples exhibit good capacitor behavior in a wide range up to 1000 mV s^{-1}, with a symmetrical

rectangular loop and a small time constant (represented by the small rounding corners as the polarity is reversed). The MnO_2 redox peaks are not observed distinctly, implying that electrodes behave as faradaic pseudocapacitors whose voltammograms consist of many fast and reversible successive surface redox reactions overlapped with each other.[44] This is also supported by EIS, showing steep rise in the imaginary axis and very low charge-transfer resistance and negligible serial resistance (< 2 Ohm) (Figure S5); a significant improvement over previous work completed by our group, due in part to the use of a Ti substrate in lieu of the thin Cr film coated Silicon wafer.[30] In general, the SC value monotonically decreases as the nominal Mn thickness is increased (Figure 4c). At 1 mV s^{-1} scan rate, the 600 nm sample provided 162 F g^{-1}, while the 100 nm sample sailed to a notable 437 F g^{-1}. Increasing the scan rate up to 1000 mV s^{-1} only caused the SC value to descend to 76 F g^{-1} and 135 F g^{-1}, respectively. Pushing the scan rate further to 2000 mV s^{-1} caused the SC to fall more quickly, but still able to deliver a surprising 54 F g^{-1} and 109 F g^{-1}, respectively. Although the capacitance of the MnO_2-coated VACNFs seems to follow a logarithmic trend with increasing scan rate (Figure 4c), it is noteworthy that such large SC values at a scan rate of 2000 mV s^{-1} (corresponding to 2.5 Hz) is rarely reported for supercapacitors in the literature. In comparison, the control experiment with a planar 50 nm thick Mn film on Cr-coated Si wafer only matches the SC value of the worst sample (600 nm nominal thickness) of all Mn-coated VACNFs at 1.0 mV s^{-1}, but decreased more significantly to 22.1 F g^{-1} at 1000 mV s^{-1} (Figure 4c). This result illustrates that the nanoscale architecture provided by the VACNFs is indeed critical to the better performance.

FIGURE 5

The charge-discharge capability at high current densities is one of the most important factors in the development of new electrodes for supercapacitors. Following cyclic voltammetry, a series of chronopotentiometric measurements were performed at a current density of 0.27 A g^{-1} to 140 A g^{-1}. Figure 5a shows the rate capability of the electrode with 300 nm nominal thickness, at 0.28, 2.78, and

28.7 A g^{-1}, respectively. The nearly linear and symmetric feature of the voltage profiles suggests good capacitor behavior of the MnO_2-coated VACNF arrays. The corresponding SC values can be calculated as 246, 127, and 97 A g^{-1} by SC = (i_c x t)/ΔV where i_c is the charge (or discharge current density), t the charge (or discharge time), and ΔV the potential window. The SC value only dropped by about a factor of 2.5 as the current density was raised by 100 times, indicating the high reaction rate which matches the high current density.

Figure 5b shows the charge-discharge curves at 2.78 A g^{-1} for the four samples with 100, 200, 300, and 600 nm nominal Mn thickness. Similar to the CV measurements, the SC value gradually decreases as the thickness of MnO_2 is increased, achieving a capacitance of 250 F g^{-1} for the 100 nm nominal electrode, decreasing to 127 F g^{-1} for the 600 nm nominal electrode. This reveals that while mass loading increases, the thicker MnO_2 shell was not fully utilized. However, even the sample with 600 nm nominal Mn thickness was able to achieve a SC of 61 F g^{-1} at an extremely large current of ~110 A g^{-1} (Figure 5c). This property is well exceeding the performance of the much thinner 50 nm planar Mn film on Cr-coated Si wafer, i.e. 144.3 F g^{-1} at 0.22 A g^{-1} and 25 F g^{-1} at 22 A g^{-1}. The MnO_2-coated VACNFs at lower nominal Mn thicknesses consistently show higher SC values that drop slower at high current densities. In addition, a fresh electrode with 300 nm nominal Mn thickness was tested at 10 A g^{-1} for over 2400 cycles (Figure S6). Besides the small initial decay, the SC value of this electrode becomes extremely stable after 800 cycles, maintaining a SC of 152 F $(g_{MnO_2})^{-1}$ after 2000 cycles. The columbic efficiency over the course is over 98.5%.

FIGURE 6

From above results, it is clear that, by spreading Mn along the VACNFs as a thin shell, 12 fold of Mn (i.e. 600 nm vs. 50 nm nominal thickness) can be used while achieving better performance than that on a flat surface. This significantly increases the Mn mass loading and the total energy storage capacity. As we discussed in the introduction, the maximum thickness of MnO_2 films, either planar

film on flat surface or coaxial shell wrapping around VACNFs, is determined by both electron and ion transport properties. The high porosity of the rose-petal-like MnO_2 nanostructure formed by electrochemical oxidation in this study allows cations to easily access the entire MnO_2 material through much faster diffusion in solution than across the solid MnO_2 film. As a result, the usable radial thickness of MnO_2 shell can be expanded to over 200 nm (see Figure S2l) from the 7.5 nm compact shell in our previous study which was ion transport limited.[30] However, the low electrical conductivity of MnO_2 may now be a limiting factor, particularly in thicker shells. As illustrated in Figure 6, the outer portion of a thick MnO_2 shell may lose effective electrical connection with the CNF core and thus is not fully engaged in charge-discharge processes even though there are much more ions available in the outer portion for insertion reactions. This factor is responsible for the lower SC value as the nominal Mn thickness is increased. For the same reason, the XPS data in Figure 3a showed that the MnO_2 at the outer surface of the samples started with 100 and 300 nm nominal Mn thickness was reduced to valence state +3 at the last discharge cycle while that of the 600-nm sample remained at +4. The inner portion of the MnO_2 shell (represented by the red color in Figure 6 has much better electrical connection to the CNF core and serves as the most active redox materials during charge and discharge. Overall, this hybrid core-shell structure is expected to enhance both energy capacity and power rate of the MnO_2 supercapacitor.

FIGURE 7

To illustrate the potential of these 3D architectured hybrid electrodes for electrical energy storage, the specific energy (Wh kg^{-1}) and specific power (W kg^{-1}) of a full cell have been derived from the above half-cell results and plotted in the Ragone plot (Figure 7. For a single supercapacitor electrode, the maximum stored energy is related to the total Q built up on the electrode in a linear fashion up to the maximum voltage V, with:

$$C_0 = \frac{Q}{Vm} \qquad E_0 = (1/2)C_0V^2$$

(6) (7)

However, for a full cell consisting of two identical electrodes, the specific energy is represented by the following:

$$E_{0,full\ cell} = (1/8)C_0V^2 \quad (8)$$

The specific power P_0 of a supercapacitor represents the maximum power output at the voltage limit, which can be calculated by

$$P_0 = \frac{V^2}{4\ m\ ESR} \quad (9)$$

where ESR is the equivalent series resistance that is determined by the voltage drop after the current polarity is flipped during charge-discharge processes.

Interestingly, as the current density was varied by 100 fold, from ~0.28 A g^{-1} to ~28 A g^{-1} in galvanostatic charge-discharge, the specific power *P* remained nearly constant, indicating that the change in ESR is negligible in this wide current ranges (Figure 7a). This is quite different from common supercapacitors. As shown in Figure 7b, while the specific energy in this study is between 1 to 10 Wh kg^{-1}, comparable to commercial supercapacitors[45] and compact MnO_2 shells on VACNFs in our own previous study[30], the specific power is more than one order of magnitude higher than the other studies (Figure 7b), reaching 240 kW kg^{-1} for the 100 nm nominal thickness and over 70 kW kg^{-1} for the 600 nm nominal thickness. This greatly surpasses the target in specific power of 15 kW kg^{-1} (but including the whole system), proposed by the Partnership for a New Generation of Vehicles (PNGV).[46] The high-power capability can be attributed to the improvement in ion diffusion through the electrolyte penetrating into mesoporous MnO_2 shell in the t hybrid structure. The specific energy, however, is limited by the low electrical conductivity that prevents effective electrical connection to the outer shells. Improving Mn coating to spread it more uniformly along the VACNFs and incorporating an

additional conductive polymer (or carbon) coating at electrolyte/MnO_2 interface may enhance the specific energy in future studies.

Conclusion

We have demonstrated the formation of rose-petal-like mesoporous MnO_2 layers by electrochemical oxidization of Mn shells of 100 to 600 nm nominal thickness sputter-coated on vertically aligned carbon nanofibers (VACNFs). Such 3D MnO_2/VACNF hybrid architecture provides enhanced ion diffusion across the mesoporpous MnO_2 shell and yields excellent current collecting capability using the conductive VACNF core, both required for high-performance supercapacitors. The enhanced ion diffusion lift the previous limit of optimum MnO_2 shell thickness at ~7.5 nm while the high electron and ion transport collectively enabled the fast redox reaction in thick MnO_2 shells up to 200 nm during charge-discharge processes in 1 M Na_2SO_4 electrolyte. More than one order of magnitude higher specific power (~240 kW kg^{-1}) was obtained with such a hybrid electrode material as compared to the state-of-the-art supercapacitors based on other MnO_2 structures at the similar specific energy range (~1 to 10 Wh kg^{-1}). This design strategy clearly demonstrates the remarkable capability of using VACNFs core structure as a template for high-powered energy storage devices.

Acknowledgements

The work at Kansas State University was supported by NSF grant CMMI-1100830, NASA grant NNX13AD42A, NSF EPSCoR Award EPS-0903806, and matching funds provided by the state of Kansas for the latter two. The authors would like to acknowledge Nicoleta Ploscariu for her assistance.

References

1. D. V. Ragone, *Review of battery systems for electrically powered vehicles*, SAE Technical Paper, 1968.
2. M. Lu, F. Beguin and E. Frackowiak, *Supercapacitors: Materials, Systems and Applications*, John Wiley & Sons2013.
3. P. Simon and Y. Gogotsi, *Accounts Chem. Res.*, 2012, **46**, 1094-1103

4. I. V. Barsukov, *New Carbon Based Materials for Electrochemical Energy Storage Systems: Batteries, Supercapacitors and Fuel Cells: Batteries, Supercapacitors and Fuel Cells*, Springer2006.
5. A. Barroso-Bogeat, M. Alexandre-Franco, C. Fernandez-Gonzalez, A. Macias-Garcia and V. Gomez-Serrano, *Physical chemistry chemical physics : PCCP*, 2014, **16**, 25161-25175.
6. G. Wang, L. Zhang and J. Zhang, *Chem. Soc. Revs.*, 2012, **41**, 797-828.
7. G. Yu, X. Xie, L. Pan, Z. Bao and Y. Cui, *Nano Energy*, 2013, **2**, 213-234.
8. C.-C. Hu, K.-H. Chang, M.-C. Lin and Y.-T. Wu, *Nano Lett.*, 2006, **6**, 2690-2695.
9. M. Toupin, T. Brousse and D. Bélanger, *Chem. Mater.*, 2004, **16**, 3184-3190.
10. P. Simon and Y. Gogotsi, *Nature Mater.*, 2008, **7**, 845-854.
11. D. R. Rolison, J. W. Long, J. C. Lytle, A. E. Fischer, C. P. Rhodes, T. M. McEvoy, M. E. Bourg and A. M. Lubers, *Chem. Soc. Rev.*, 2009, **38**, 226-252.
12. Z. Lei, J. Zhang and X. S. Zhao, *J. Mater. Chem. A*, 2012, **22**, 153-160.
13. J. Desilvestro and O. Haas, *J Electrochem. Soc.*, 1990, **137**, 5C-22C.
14. D. M. Adams, L. Brus, C. E. D. Chidsey, S. Creager, C. Creutz, C. R. Kagan, P. V. Kamat, M. Lieberman, S. Lindsay and R. A. Marcus, *J. Phys. Chem. B*, 2003, **107**, 6668-6697.
15. R. Huggins, *Advanced batteries: materials science aspects*, Springer2008.
16. Y. Yang, J. Choi and Y. Cui, in *Functional Metal Oxide Nanostructures*, eds. J. Wu, J. Cao, W.-Q. Han, A. Janotti and H.-C. Kim, Springer New York2012, vol. 149, ch. 12, pp. 269-302.
17. J. E. Weston and B. C. H. Steele, *J. Appl. Electrochem.*, 1980, **10**, 49-53.
18. W. Chen, R. B. Rakhi, Q. Wang, M. N. Hedhili and H. N. Alshareef, *Advanced Functional Materials*, 2014, **24**, 3130-3143.
19. F. Li, Y. Xing, M. Huang, K. L. Li, T. T. Yu, Y. X. Zhang and D. Losic, *Journal of Materials Chemistry A*, 2015, 10.1039/C1035TA00634A
20. K. Zhang, X. Han, Z. Hu, X. Zhang, Z. Tao and J. Chen, *Chemical Society Reviews*, 2015, **44**, 699-728.
21. Z. Fan, J. Chen, M. Wang, K. Cui, H. Zhou and Y. Kuang, *Diam. Relat. Mater.*, 2006, **15**, 1478-1483.
22. S.-B. Ma, K.-Y. Ahn, E.-S. Lee, K.-H. Oh and K.-B. Kim, *Carbon*, 2007, **45**, 375-382.
23. J. Yan, Z. Fan, T. Wei, J. Cheng, B. Shao, K. Wang, L. Song and M. Zhang, *J. Power Sources*, 2009, **194**, 1202-1207.
24. M. Zhi, C. Xiang, J. Li, M. Li and N. Wu, *Nanoscale*, 2013, **5**, 72-88.
25. K.-W. Nam, C.-W. Lee, X.-Q. Yang, B. W. Cho, W.-S. Yoon and K.-B. Kim, *J. Power Sources*, 2009, **188**, 323-331.
26. S. L. Chou, J. Z. Wang, S. Y. Chew, H. K. Liu and S. X. Dou, *Electrochem Commun*, 2008, **10**, 1724-1727.
27. S. W. Lee, J. Kim, S. Chen, P. T. Hammond and Y. Shao-Horn, *ACS Nano*, 2010, **4**, 3889-3896.
28. H. Zhang, G. Cao, Z. Wang, Y. Yang, Z. Shi and Z. Gu, *Nano Lett.*, 2008, **8**, 2664-2668.
29. R. Amade, E. Jover, B. Caglar, T. Mutlu and E. Bertran, *J. Power Sources*, 2011, **196**, 5779-5783.
30. J. Liu, J. Essner and J. Li, *Chem. Mater.*, 2010, **22**, 5022-5030.
31. Z. F. Ren, Z. P. Huang, J. W. Xu, J. H. Wang, P. Bush, M. P. Siegal and P. N. Provencio, *Science*, 1998, **282**, 1105-1107.
32. B. A. Cruden, A. M. Cassell, Q. Ye and M. Meyyappan, *J. Appl. Phys.*, 2003, **94**, 4070-4078.
33. A. V. Melechko, V. I. Merkulov, T. E. McKnight, M. A. Guillorn, K. L. Klein, D. H. Lowndes and M. L. Simpson, *J. Appl. Phys.*, 2005, **97**, 41301-41301-41339.
34. M. Meyyappan, L. Delzeit, A. Cassell and D. Hash, *Plasma Sources Sci. T.*, 2003, **12**, 205-216.

35. S. A. Klankowski, R. A. Rojeski, B. A. Cruden, J. Liu, J. Wu and J. Li, *J. Mater. Chem. A*, 2013, **1**, 1055-1064.
36. S. A. Klankowski, G. P. Pandey, B. A. Cruden, J. Liu, J. Wu, R. A. Rojeski and J. Li, *J. Power Sources*, 2015, **276**, 73-79.
37. Q. Ngo, T. Yamada, M. Suzuki, Y. Ominami, A. M. Cassell, J. Li, M. Meyyappan and C. Y. Yang, *IEEE T Nanotechnol*, 2007, **6**, 688-695.
38. M. Pourbaix, *Atlas of electrochemical equilibria in aqueous solutions*, National Association of Corrosion Engineers, 1974.
39. G. Rayner-Canham and T. Overton, *Descriptive inorganic chemistry*, Macmillan2003.
40. J. N. Broughton and M. J. Brett, *Electrochim Acta*, 2004, **49**, 4439-4446.
41. B. Djurfors, J. N. Broughton, M. J. Brett and D. G. Ivey, *J. Power Sources*, 2006, **156**, 741-747.
42. M. Chigane and M. Ishikawa, *J Electrochem Soc*, 2000, **147**, 2246-2251.
43. M. Chigane, M. Ishikawa and M. Izaki, *J Electrochem Soc*, 2001, **148**, D96-D101.
44. P. Simon and Y. Gogotsi, *Nature materials*, 2008, **7**, 845-854.
45. C. Huang, N. P. Young and P. S. Grant, *J. Mater. Chem. A*, 2014, **2**, 11022-11028.
46. B. E. E. Systems, C. E. T. Systems, S. C. R. R. P. P. N. G. Vehicles, N. R. Council, T. R. Board and D. E. P. Sciences, *Review of the Research Program of the Partnership for a New Generation of Vehicles:: Sixth Report*, National Academies Press2000.

Figures

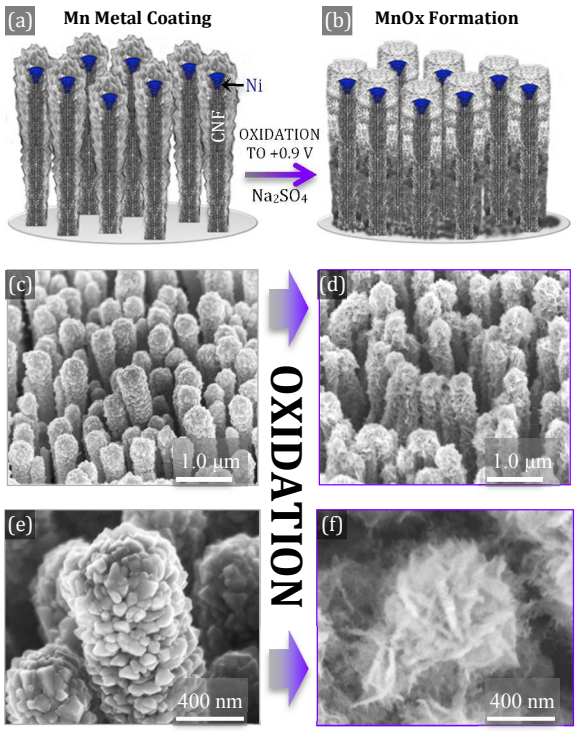

Figure 1. Schematic of Mn-coated VACNFs (a) before and (b) after electrochemical oxidation in 1 M Na_2SO_4. Representative SEM images of 300 nm nominal Mn thickness at different magnifications with (c) & (e) before oxidation and (d) & (f) after oxidation.

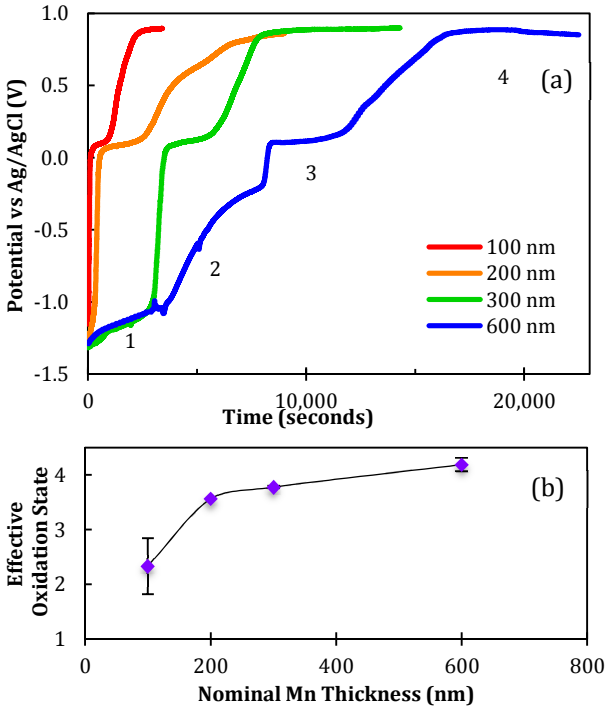

Figure 2. (a) Chronopotentiometric oxidation profiles of Mn-coated VACNF electrodes with nominal thickness of 100, 200, 300, and 600 nm, respectively. The oxidation current is fixed at 127 μA cm^{-2} with an upper limit of +0.9 V. (b) The average effective oxidation state calculated from the profile of chronopotentiometric oxidation of Mn to MnO_2.

Table 1. Summary of the Mn 3s XPS features

Sample	Mn 3s Spectra Values		
(Nominal)	E_B(main)/eV	E_B(sat)/eV	ΔE_B/eV
100 nm MnO_x	83.57	88.80	5.23
300 nm MnO_x	83.54	88.86	5.32
600 nm MnO_x	84.00	88.64	4.64

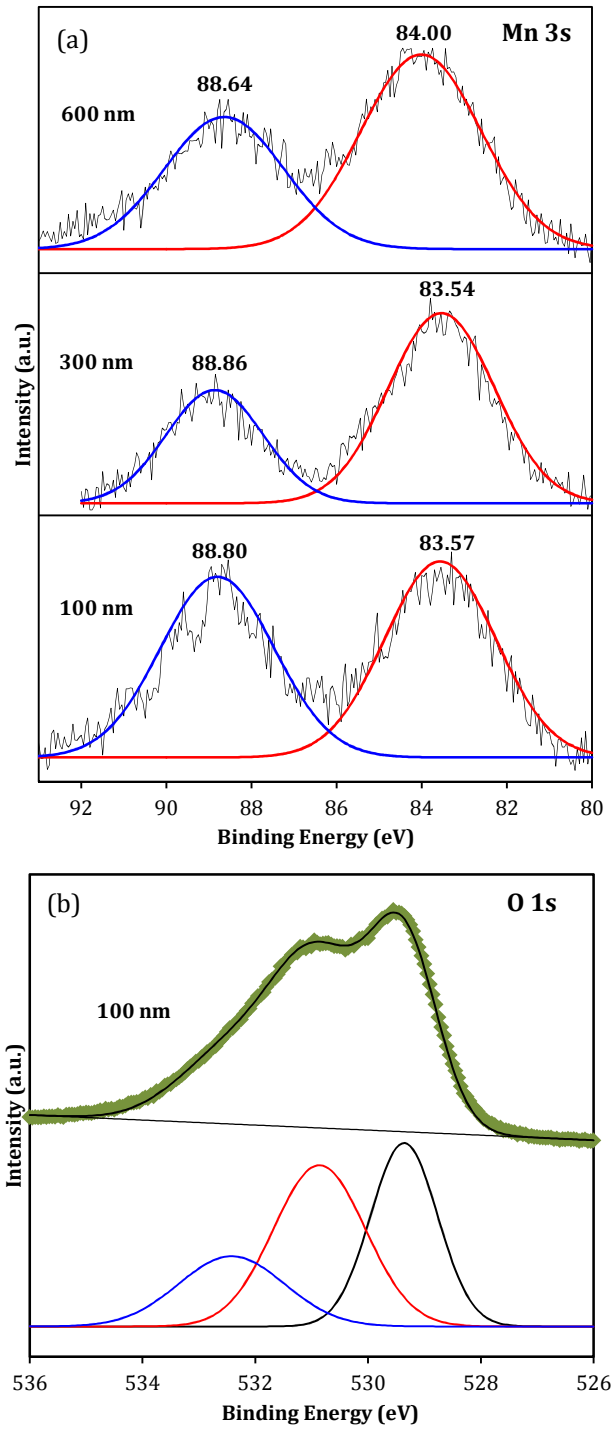

Figure 3. (a) Mn 3s core level XPS spectra for 100, 300 and 600 nm MnO_2-coated VACNF electrodes. The peak separation values are indicated. The raw data is represented by black line, and the fitted data are represented by blue and red lines. (b) A typical O 1s spectra (green diamonds) along with fittings for H-O-H (blue), Mn-OH (red), and Mn-O-Mn (black) bindings for 100 nm MnO_2 coated VACNF electrode.

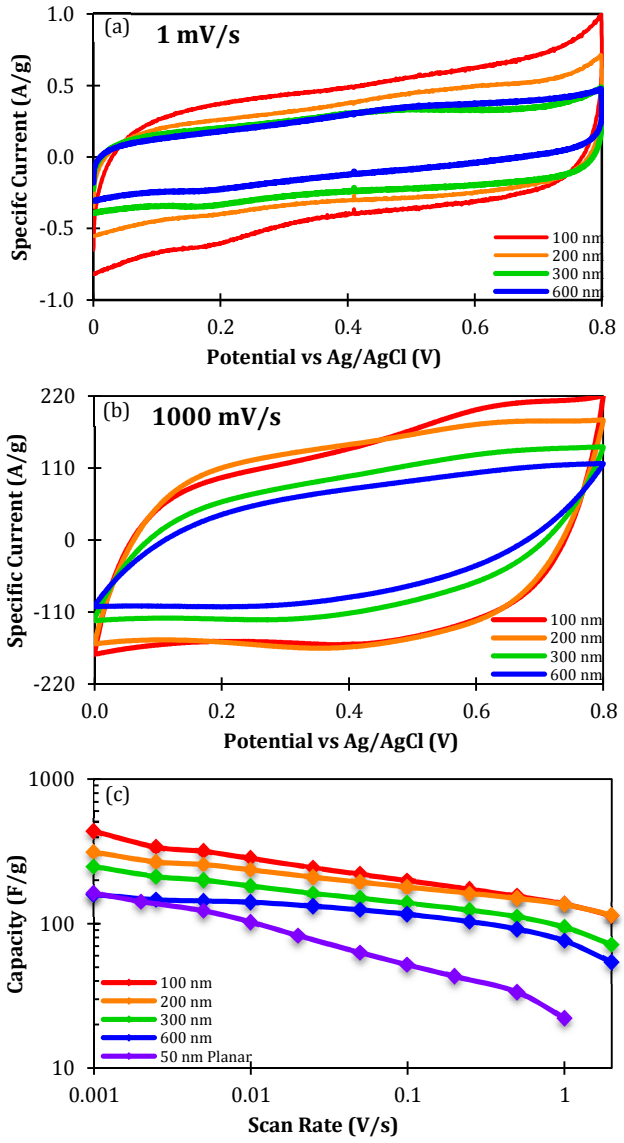

Figure 4. I-V curves by cyclic voltammetry for Mn-coated VACNF electrodes with nominal thickness of 100, 200, 300, and 600 nm, performed at the scan rate of (a) 1.0 mV/s and (b) 1000 mV/s. (c) The specific capacity versus the scan rate for various nominal thicknesses. The curve labeled as "50 nm Planar" is measured with a control sample of 50 nm thick planar Mn film deposited on a flat Cr-coated Si wafer.

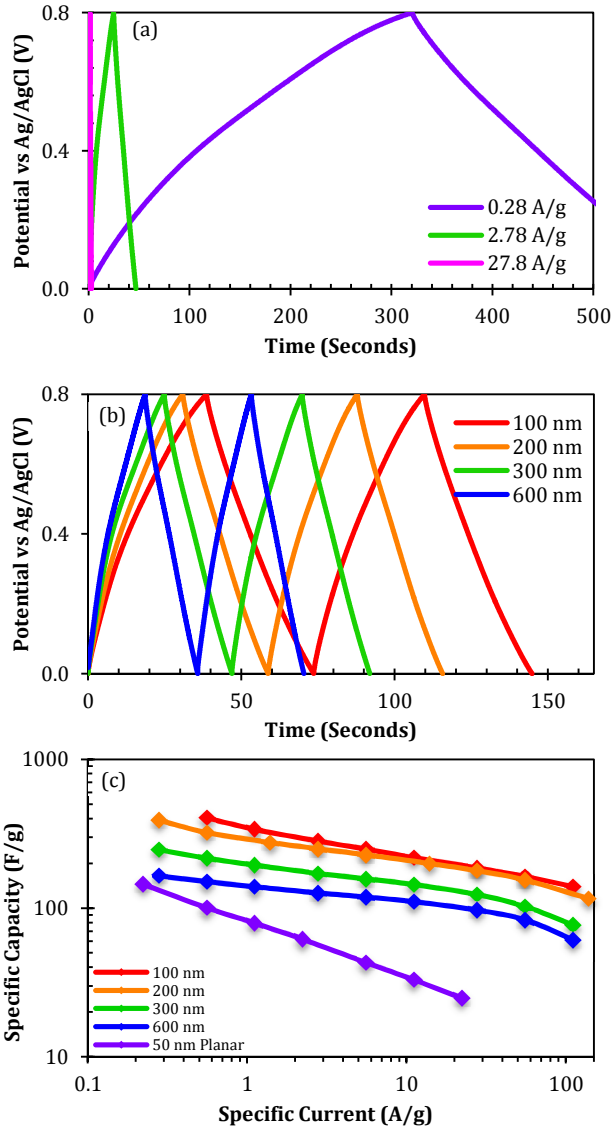

Figure 5. Chronopotentiometric cycling profiles of Mn-coated VACNF electrode with (a) 300 nm nominal thickness at 0.28 A g^{-1}, 2.78 A g^{-1}, and 27.8 A g^{-1} and comparison (b) with varied nominal thickness of 100, 200, 300, and 600 nm all at 2.78 A g^{-1}. (c) Logarithm-logarithm curve of specific capacitance versus specific current rate for various nominal thicknesses.

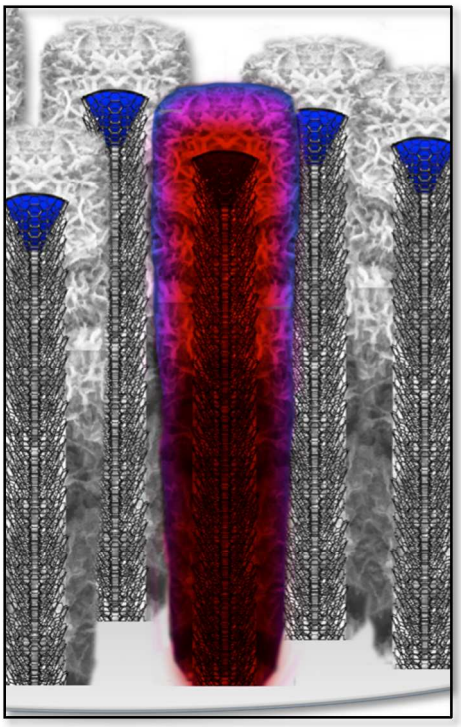

Figure 6. Schematic illustration of the variation in electrochemical activity in MnO_2-coated VACNFs. The inner portion is highly active (**red**) while the outer portion is less active (**blue**) due to the low electrical conductivity of MnO_2.

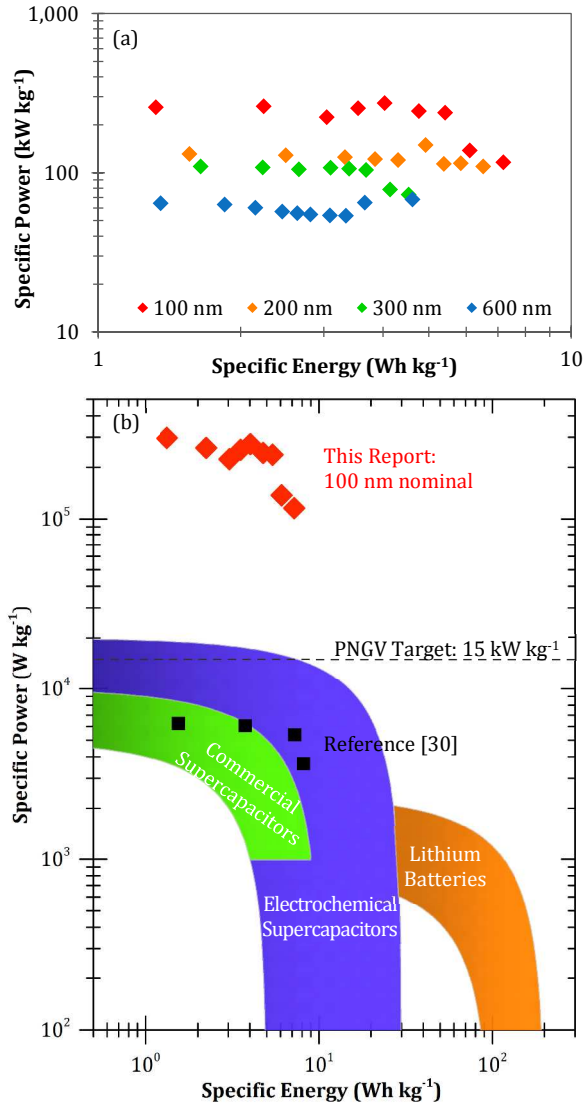

Figure 7. Ragone plots of Mn-coated VACNF electrodes (a) at the nominal Mn thicknesses of 100, 200, 300, and 600 nm; and (b) at 100 nm nominal Mn thickness (◆) with comparisons to values achieved in previous work [30] (■), and the range seen for commercial & state-of-art supercapacitors and as well as lithium based batteries [40]. The black dashed line represents a target in specific power proposed by Partnership for a New Generation of Vehicles (PNGV) [46].